

PAPER

Behavior of argon gas release from manganese oxide minerals as revealed by $^{40}\text{Ar}/^{39}\text{Ar}$ laser incremental heating analysis

LI Jianwei¹, P. M. Vasconcelos² & ZHANG Jun¹

1. Faculty of Earth Resources, China University of Geosciences, Wuhan 430074, China;

2. Department of Earth Sciences, The University of Queensland, Brisbane 4072, Australia

Correspondence should be addressed to LI Jianwei (e-mail: 11209@public.wh.hb.cn)

Abstract Manganese oxides in association with paleo-weathering may provide significant insights into the multiple factors affecting the formation and evolution of weathering profiles, such as temperature, precipitation, and biodiversity. Laser probe step-heating analysis of supergene hollandite and cryptomelane samples collected from central Queensland, Australia, yield well-defined plateaus and consistent isochron ages, confirming the feasibility dating very-fined supergene manganese oxides by $^{40}\text{Ar}/^{39}\text{Ar}$ technique. Two distinct structural sites hosting Ar isotopes can be identified in light of their degassing behaviors obtained by incremental heating analyses. The first site, releasing its gas fraction at the laser power 0.2–0.4 W, yields primarily $^{40}\text{Ar}_{\text{atm}}$, $^{38}\text{Ar}_{\text{atm}}$, and $^{36}\text{Ar}_{\text{atm}}$ (atmospheric Ar isotopes). The second sites yield predominantly $^{40}\text{Ar}^*$ (radiogenic ^{40}Ar), $^{39}\text{Ar}_K$, and $^{38}\text{Ar}_K$ (nucleogenic components), at ~0.5–1.0 W. There is no significant Ar gas released at the laser power higher than 1.0 W, indicating the breakdown of the tunnel sites hosting the radiogenic and nucleogenic components. The excellent match between the degassing behaviors of $^{40}\text{Ar}^*$, $^{39}\text{Ar}_K$, and $^{38}\text{Ar}_K$ suggests that these isotopes occupy the same crystallographic sites and that $^{39}\text{Ar}_K$ loss from the tunnel site by recoil during neutron irradiation and/or bake-out procedure preceding isotopic analysis does not occur. Present investigation supports that neither the overwhelming atmospheric ^{40}Ar nor the very-fined nature of the supergene manganese oxides poses problems in extracting meaningful weathering geochronological information by analyzing supergene manganese oxides minerals.

Keywords: hollandite, cryptomelane, $^{40}\text{Ar}/^{39}\text{Ar}$ laser incremental heating, argon degassing, tunnel site.

Chemical weathering in the Earth planet has played significant roles in the formation and evolution of landscapes and supergene enrichments of ore deposits. However, chronology of weathering profiles has long been established on identification of stratigraphic relationships of weathering profiles to the underlying and/or overlying units whose geological ages are well constrained, and more recently, on some geochronological approaches such

as paleomagnetic and stable isotopic dating methods^[1,2]. Nevertheless, the young ages of many weathering crusts are beyond the useful limits of the techniques above. Other techniques either are inapplicable because of the lack of datable minerals contained in weathering profiles or unreliable because they require assumptions about element immobility after incorporation into the weathering crusts^[3]. Thus, direct and precise dating of weathering profiles is necessary and imperative to help unravel the complex history of continental weathering. Modern laser incremental heating $^{40}\text{Ar}/^{39}\text{Ar}$ method has been successfully applied to the study of very small grains from various geological environments^[4,5]. The fine resolution possible with this method makes it uniquely suited to the study of the distribution of distinct Ar isotopes within the analyzed minerals^[6,7].

Manganese oxides are ubiquitous in weathering profiles, and may potentially be dated by K-Ar and $^{40}\text{Ar}/^{39}\text{Ar}$ methods^[5,8,9]. The hollandite-group minerals, the most common manganese oxides in manganiferous crusts, have the general formula $A_{1-2}B_8\text{O}_{16} \cdot x\text{H}_2\text{O}$. The A site can be occupied by large cations such as K^+ , Ba^{2+} , Na^+ , Cu^+ , Pb^{2+} , Rb^{2+} , Sr^{2+} , etc., whereas the B site hosts Mn^{3+} , Mn^{4+} , Fe^{3+} , Al^{3+} , Si^{4+} , Co^{2+} , and Mg^{2+} . The identity of the A-cation determines the mineral species, with hollandite and cryptomelane as the Ba and K end-members, respectively^[10]. B-cations (commonly Mn^{4+}) octahedrally share edges^[11]. Vertice-sharing double chains form large channels (tunnel sites) partially filled by H_2O and A-cations in eightfold coordination with oxygen atoms from the double chains^[11]. The large spaces within the tunnels sites can accommodate large Ar (0.196 nm radius) atoms derived from the radioactive decay of K and may also host atmospheric argon either as trapped air component or as Ar dissolved in tunnel H_2O . The tunnel sites may also potentially host other dissolved constituents from paleo-weathering solutions (e.g. Cl^- ions).

The pioneering work performed by Vasconcelos^[6] demonstrates that the hollandite-group manganese minerals are amenable to $^{40}\text{Ar}/^{39}\text{Ar}$ isotopic dating. He employed the laser probe $^{40}\text{Ar}/^{39}\text{Ar}$ technique to successfully date cryptomelane from deeply weathered pegmatites in southeast Brazil. Subsequent efforts have added substantial weight of evidence in support of the promising hollandite-group Mn-oxides as a datable phase by $^{40}\text{Ar}/^{39}\text{Ar}$ method^[12–17]. However, the greatest challenges in precisely dating manganese oxides lie in the very-fined habit of supergene Mn-oxides and associated ^{39}Ar recoil during neutron irradiation and bake-out procedure; the possible loss of K/Ar from the Mn-oxide structures due to diffusion or exchange with ground waters; and the contamination of supergene minerals by hypogene phases and the

resultant incorporation of excess ^{40}Ar into the structures of supergene minerals.

This study presents results of $^{40}\text{Ar}/^{39}\text{Ar}$ analysis of hollandite and cryptomelane samples collected from Queensland, Australia. The laser step-heating analyses confirm that both samples were stable and Ar-retentive during neutron irradiation and bake-out procedure preceding mass spectrometric analysis. The analyses also permit us to identify the respective contributions of argon fractions from different reservoirs (adsorbed gas, intercrystalline space, intracrystalline sites, etc.) in cryptomelane and hollandite (fig. 1). The distinct thermal behavior of these reservoirs allows us to measure each isotope group separately, helping to define the laser power level where most radiogenic and nucleogenic components are released, and meaningful geochronological information on paleoweathering can be retrieved.

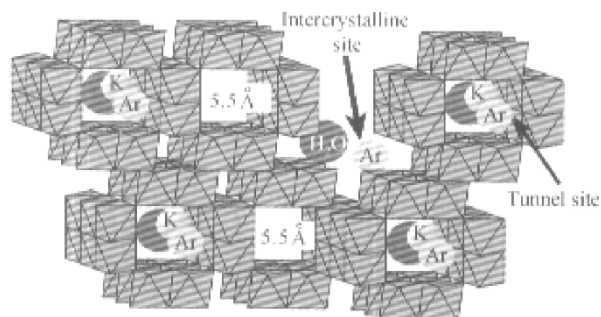


Fig. 1. Diagrammatic illustration of the hollandite-group structures, showing the tunnel site occupied by the large K⁺, Ar molecular, and tunnel H₂O. Other large cations such as Ba and Pb are not shown. The intercrystalline sites occupied by Ar and H₂O are also shown (modified from Burns and Burns^[10]).

2 Samples and analytical techniques

This study investigates two distinct Mn-oxide samples, Tabor99-07 and Tabor99-15, collected from weathering profile in central Queensland, Australia. Polished thin sections of each sample were studied by combined transmitted- and reflected-light microscopy to determine the mineralogy and paragenesis of the datable phases, and to identify the possible contamination by primary minerals (silicates, quartz, etc.). After petrographic examination, suitable parts of the samples were crushed, washed in distilled water in an ultrasonic bath for at least one hour, and dried. For each sample, 20—50 grains and clusters of visually pure Mn oxides ranging from 0.5 mm to 2 mm in diameter were handpicked under a binocular microscope. Three to five grains from each sample were mounted in an epoxy container and polished for scanning electron microscopy (SEM) and electron microprobe (EMP) analysis. The mounted grains were carbon coated and investigated with a JEOL JXA 8800L Superprobe at the Center for Microscopy and Microanalysis at the University of

Queensland. Standards and unknowns were analyzed with 0.5 μm beam diameter at 15 kV and 15 nA current. On the basis of EMP and SEM investigations, ten to twenty monomineralic and relatively K-rich grains from each sample were loaded into irradiation disks along with the Fish Canyon standards (nominal age of 28.02 Ma)^[18]. The disks were wrapped in Al-foil, vacuum-sealed in silica glass tubes and irradiated for 14 h at the B-1 CLICIT facility at the Radiation Centre, Oregon State University, USA. Sample and flux monitor irradiation geometry followed those of Vasconcelos^[12]. After a two-month cooling period, the samples were analyzed by the laser incremental-heating $^{40}\text{Ar}/^{39}\text{Ar}$ method employing a MAP215 noble gas mass spectrometer hosting at the UQ-AGES (University of Queensland Argon Geochronology in Earth Sciences) laboratory, following procedures detailed by Vasconcelos^[12]. For each sample, three grains (Tabor99-07/01&02&03 and Tabor99-15/01&02&03) were isotopically analyzed to test the reproducibility of chronological results.

3 Results

Petrographic and SEM observations reveal that the manganese oxides are visually pure, porous, characterized by the conspicuous botryoidal texture composed of acicular cryptomelane and hollandite (fig. 2), indicating a pre-

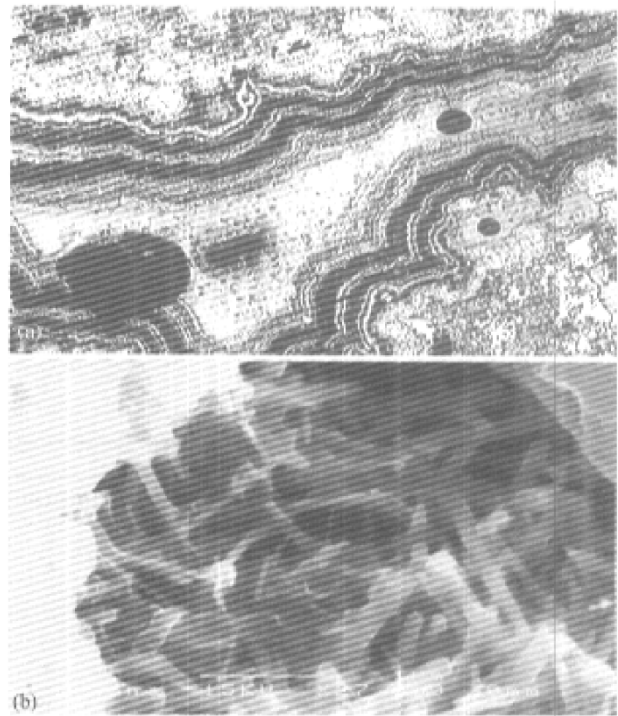


Fig. 2. Photomicrographs showing the botryoidal texture of the manganese oxides investigated (a) and the acicular cryptomelane (b). Note the very fine and porous habits of the oxides. Field of view in (a) is approximately 1.5 mm.

cipitation mode of cavities filling and reflecting high degree of crystallinity. These results, in combination with subsequent EMP analysis, suggest that Tabor99-07 consists of hollandite, whereas cryptomelane dominates in the Tabor99-15 sample. Fig. 3 illustrates the results obtained by EMP analyses. The hollandite sample is characterized by relatively high Ba concentration and relatively low K contents, whereas cryptomelane sample owns high K concentration and is also rich in Ba (fig. 3(a), (c)). The totals of EMP analysis are generally between 94% and 99%, mostly resulting from the micro-porous nature of the Mn-oxides (fig. 2(b)). The EMP analysis also reveals existence of H₂O present in the cryptomelane and hollandite samples, ranging from 1.2% to 3.4% and potentially containing dissolved atmospheric Ar. The Mn contents of the samples analyzed are generally 24%—45% and 40%—50%, respectively (fig. 3(b), (d)). Variation of Mn concentration largely stems from the different contents of trace elements present within the *B* site of the Mn-oxides, including Co, Al, Si, etc. The inverse correlations between Mn and Fe+Si+Al contents (fig. 3(b), (d)) suggest competition between Mn and these elements for the *B* site. Reflected-light microscopy, SEM, and EMP analysis consistently indicate that the samples are K-rich, monomineralic, and well crystallized, and thus suitable for ⁴⁰Ar/³⁹Ar analysis.

The analytical results of argon isotopes are tabulated in table 1. Fig. 4 illustrates step-heating spectra, isotope correlation diagrams, and ideogram for each grain. An ideogram is the probability density plot of a set of dates, and an ideogram age means the most probable age inferred from a series analyses. These figures permit the

identification of the major weathering ages and the quick evaluation on the quality of the analyses.

The well-defined plateaus, where six or more contiguous steps containing more than 80% of the total amount of ³⁹Ar_K released, yield chronological results reproducible at the 95% confidence level (2σ) (fig. 4(a)–(f)). The shapes of the step-heating spectra, however, indicate very large uncertainties in the initial steps of analysis, and this will be discussed below. Calculated integrated ages and isochron ages for six grains from these two samples show very good agreement with the corresponding plateau ages (fig. 4(a)–(h)), though the integrated ages have relatively large errors. The excellent concordance between the plateau, integrated, and isochron ages is indicative of the point that neither K nor Ar has lost during the sample history, attesting the reliability of the present ⁴⁰Ar/³⁹Ar results. The corresponding intercepts (⁴⁰Ar/³⁶Ar) are around 295—296 (fig. 4(g)–(h)), in good agreement with the present-day atmospheric value, and indicating no excess argon incorporated in the samples dated.

Due to the similarity of argon gas release behavior among different grains, subsequent discussions will be focused on a representative grain from each sample (Tabor99-07/01 and Tabor99-15/02, respectively). The Ar release history of representative grain of the hollandite (Tabor99-07/01) and cryptomelane (Tabor99-15/02) samples are shown in figs. 5 and 6. The degassing history of both samples shows remarkable similarity, although small discrepancy is noticeable. During step-heating, a majority of atmospheric ⁴⁰Ar (⁴⁰Ar_{atm}) is released at a narrow range of low laser power (0.20—0.40 W). There is 25%—35% of ⁴⁰Ar_{atm} released upon heated (i.e. the first heating step

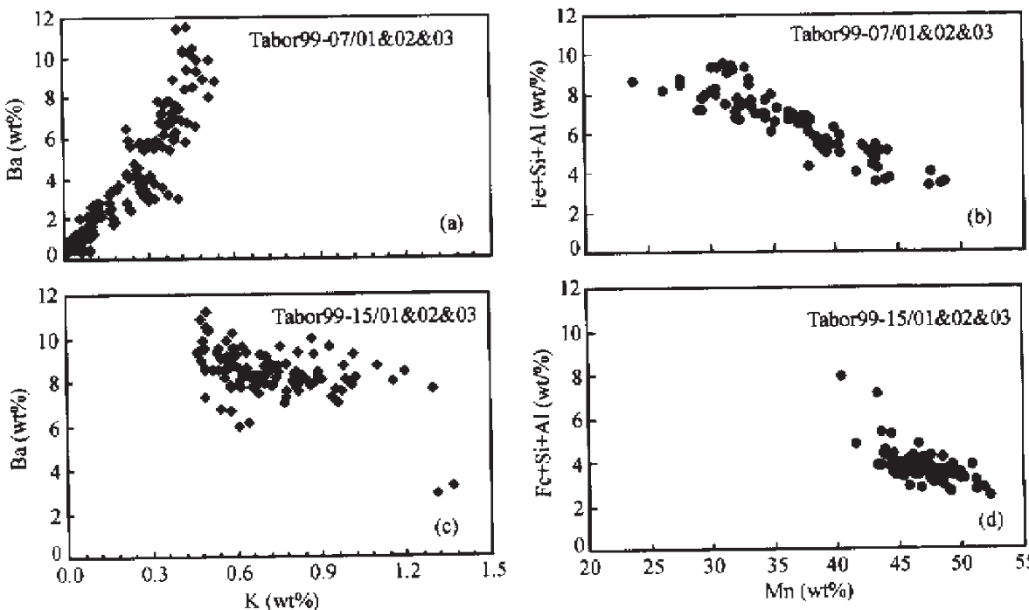


Fig. 3. Elemental correlations from electron microprobe analysis.

Table 1 Results of $^{40}\text{Ar}/^{39}\text{Ar}$ laser incremental heating analysis^{a)}

Run ID#	Power /W	$^{40}\text{Ar}^*$ /mol	$^{40}\text{Ar}_{\text{Ium}}$ cum. % ^{b)}	$^{40}\text{Ar}_{\text{Ium}}$ /mol	$^{39}\text{Ar}_{\text{Ium}}$ cum. % ^{b)}	$^{39}\text{Ar}_{\text{Ium}}$ /mol	^{38}Ar /mol	^{38}Ar cum. %	$^{38}\text{Ar}_{\text{Ium}}$ /mol	$^{38}\text{Ar}_{\text{Ium}}$ cum. %	$^{38}\text{Ar}_{\text{Ium}}$ /mol	$^{38}\text{Ar}_{\text{Ium}}$ cum. %	^{36}Ar /mol	^{36}Ar cum. %	$\Delta \text{ge/Ma} (\pm 2\sigma)$
Tabor99-07/01 ^{c)}															
1393-01A	0.20	7.54×10^{-15}	17.90	6.20×10^{-13}	35.83	2.71×10^{-16}	2.85	4.04×10^{-16}	32.84	3.93×10^{-16}	35.74	2.92×10^{-18}	3.03	7.85×10^{-18}	$24.68 \cdot 2.09 \times 10^{-15}$
1393-01B	0.25	4.87×10^{-15}	29.47	5.36×10^{-13}	66.79	5.11×10^{-16}	8.21	3.52×10^{-16}	61.44	3.40×10^{-16}	66.61	5.50×10^{-18}	8.72	6.61×10^{-18}	$45.48 \cdot 1.81 \times 10^{-15}$
1393-01C	0.30	2.16×10^{-15}	34.61	3.58×10^{-13}	87.49	6.78×10^{-16}	15.32	2.31×10^{-16}	80.25	2.27×10^{-16}	87.26	1.30×10^{-18}	10.07	2.86×10^{-18}	$54.48 \cdot 1.21 \times 10^{-15}$
1393-01D	0.40	2.95×10^{-15}	41.62	1.44×10^{-13}	95.84	9.51×10^{-16}	25.29	1.04×10^{-16}	88.73	9.18×10^{-17}	95.59	1.02×10^{-17}	20.66	2.44×10^{-18}	$62.17 \cdot 4.89 \times 10^{-16}$
1393-01E	0.50	6.84×10^{-15}	57.87	2.89×10^{-14}	97.52	2.03×10^{-15}	46.66	4.50×10^{-17}	92.38	1.83×10^{-17}	97.26	2.19×10^{-17}	43.37	4.66×10^{-18}	$76.83 \cdot 9.82 \times 10^{-17}$
1393-01F	0.59	1.15×10^{-14}	85.11	2.52×10^{-14}	98.98	3.05×10^{-15}	78.73	5.02×10^{-17}	96.46	1.60×10^{-17}	98.71	3.29×10^{-17}	77.43	1.26×10^{-18}	$80.79 \cdot 8.55 \times 10^{-17}$
1393-01G	0.69	6.18×10^{-15}	99.78	1.06×10^{-14}	99.59	1.73×10^{-15}	96.87	2.72×10^{-17}	98.67	6.75×10^{-18}	99.33	1.86×10^{-17}	96.71	1.79×10^{-18}	$86.44 \cdot 3.60 \times 10^{-17}$
1393-01H	0.84	6.19×10^{-16}	101.25	1.52×10^{-15}	99.68	2.34×10^{-16}	99.33	5.31×10^{-18}	99.10	9.67×10^{-19}	99.41	2.52×10^{-18}	99.31	1.82×10^{-18}	$92.18 \cdot 5.16 \times 10^{-18}$
1393-01I	1.99	4.19×10^{-17}	101.35	4.18×10^{-16}	99.70	3.26×10^{-17}	99.67	1.59×10^{-18}	99.23	2.65×10^{-19}	99.44	3.52×10^{-19}	99.68	9.78×10^{-19}	$95.26 \cdot 1.41 \times 10^{-18}$
1393-01J	3.18	-6.12×10^{-16}	100.00	1.24×10^{-15}	100.00	2.60×10^{-17}	100.00	2.54×10^{-18}	99.44	7.89×10^{-19}	100.00	2.80×10^{-19}	100.00	1.47×10^{-18}	$100.00 \cdot 4.21 \times 10^{-18}$
Tabor99-07/02															
1393-02A	0.20	9.91×10^{-16}	4.16	4.94×10^{-13}	54.88	4.09×10^{-16}	5.88	3.18×10^{-16}	48.78	3.13×10^{-16}	54.90	3.13×10^{-18}	5.88	1.41×10^{-18}	$1.36 \cdot 1.67 \times 10^{-15}$
1393-02B	0.25	2.98×10^{-17}	4.29	2.98×10^{-14}	88.01	5.59×10^{-16}	13.91	1.95×10^{-16}	78.83	1.89×10^{-16}	88.05	1.89×10^{-18}	13.90	4.74×10^{-18}	$5.93 \cdot 1.03 \times 10^{-15}$
1393-02C	0.30	1.07×10^{-15}	8.80	5.01×10^{-14}	93.57	4.35×10^{-16}	20.15	4.98×10^{-17}	84.94	1.17×10^{-17}	93.61	9.17×10^{-18}	20.14	2.89×10^{-17}	$33.70 \cdot 1.72 \times 10^{-16}$
1393-02D	0.40	3.47×10^{-15}	23.41	1.86×10^{-14}	95.65	8.92×10^{-16}	32.95	5.06×10^{-17}	88.10	1.01×10^{-17}	95.69	1.18×10^{-17}	32.94	2.86×10^{-17}	$61.22 \cdot 6.42 \times 10^{-17}$
1393-02E	0.50	8.29×10^{-15}	58.25	2.47×10^{-14}	98.40	2.29×10^{-15}	65.80	4.10×10^{-17}	94.39	1.57×10^{-18}	98.44	1.57×10^{-17}	65.77	2.37×10^{-17}	$84.06 \cdot 8.50 \times 10^{-17}$
1393-02F	0.59	5.23×10^{-15}	80.26	1.11×10^{-14}	99.63	1.55×10^{-15}	87.98	2.55×10^{-17}	98.31	7.03×10^{-18}	99.67	7.03×10^{-18}	87.94	1.14×10^{-17}	$95.10 \cdot 3.89 \times 10^{-17}$
1393-02G	0.69	2.12×10^{-15}	89.18	1.27×10^{-15}	99.77	4.14×10^{-16}	93.93	5.89×10^{-18}	99.21	8.08×10^{-19}	99.81	8.08×10^{-19}	93.89	4.27×10^{-18}	$98.21 \cdot 5.55 \times 10^{-18}$
1393-02H	0.85	1.21×10^{-15}	94.27	3.14×10^{-16}	99.80	2.14×10^{-16}	97.01	1.31×10^{-18}	99.41	1.99×10^{-19}	99.84	1.99×10^{-19}	96.97	9.19×10^{-19}	$99.10 \cdot 2.45 \times 10^{-18}$
1393-02I	3.18	1.38×10^{-15}	100.00	1.45×10^{-16}	100.00	2.06×10^{-16}	99.98	8.82×10^{-19}	100.00	6.23×10^{-19}	100.00	1.23×10^{-19}	$100.00 \cdot 1.34 \times 10^{-19}$	$100.00 \cdot 7.70 \times 10^{-18}$	
Tabor99-07/03															
1393-03A	0.20	3.96×10^{-15}	15.97	9.87×10^{-13}	85.10	6.28×10^{-16}	8.12	6.30×10^{-16}	77.41	6.26×10^{-16}	85.11	6.26×10^{-19}	8.13	3.86×10^{-18}	$5.85 \cdot 3.34 \times 10^{-15}$
1393-03B	0.25	3.30×10^{-15}	29.28	1.19×10^{-14}	95.36	5.94×10^{-16}	15.80	8.02×10^{-17}	87.26	7.55×10^{-17}	95.37	7.55×10^{-19}	15.81	3.95×10^{-18}	$11.82 \cdot 4.06 \times 10^{-16}$
1393-03C	0.30	3.64×10^{-16}	30.75	3.00×10^{-14}	97.95	6.17×10^{-16}	23.78	2.66×10^{-17}	90.53	1.90×10^{-17}	97.96	1.90×10^{-18}	23.80	5.70×10^{-18}	$20.45 \cdot 1.02 \times 10^{-16}$
1393-03D	0.40	4.62×10^{-15}	49.38	1.05×10^{-14}	98.86	1.99×10^{-15}	49.54	2.84×10^{-17}	94.02	6.68×10^{-18}	98.87	6.68×10^{-18}	49.57	1.50×10^{-17}	$43.22 \cdot 3.58 \times 10^{-17}$
1393-03E	0.50	7.56×10^{-15}	79.85	5.89×10^{-15}	99.37	2.25×10^{-15}	78.70	3.01×10^{-17}	97.71	3.73×10^{-18}	99.38	3.73×10^{-18}	78.76	2.26×10^{-17}	$77.45 \cdot 1.99 \times 10^{-17}$
1393-03F	0.59	3.01×10^{-15}	92.00	1.30×10^{-15}	99.48	8.89×10^{-16}	90.20	9.77×10^{-18}	98.91	8.28×10^{-19}	99.49	8.28×10^{-19}	90.26	8.12×10^{-18}	$89.73 \cdot 4.42 \times 10^{-18}$
1393-03G	0.69	9.85×10^{-16}	95.98	8.70×10^{-16}	99.56	4.35×10^{-16}	95.82	4.76×10^{-18}	99.50	5.52×10^{-19}	99.57	5.52×10^{-19}	95.89	3.66×10^{-18}	$95.28 \cdot 2.94 \times 10^{-18}$
1393-03H	0.84	6.09×10^{-16}	98.43	2.98×10^{-16}	99.58	2.21×10^{-16}	98.68	2.51×10^{-18}	99.80	1.89×10^{-19}	99.59	1.89×10^{-19}	98.75	2.13×10^{-18}	$98.52 \cdot 1.01 \times 10^{-18}$
1393-03I	3.18	3.19×10^{-15}	100.00	4.41×10^{-15}	100.00	1.01×10^{-16}	100.00	1.42×10^{-18}	100.00	1.79×10^{-19}	100.00	2.79×10^{-18}	$100.00 \cdot 9.63 \times 10^{-19}$	$100.00 \cdot 2.61 \times 10^{-18}$	

(To be continued on the next page)

Continued)

Run ID#	Power /W	$^{40}\text{Ar}^*$ /mol	cum.% ^a	$^{40}\text{Ar}_{\text{fam}}$ /mol	$^{40}\text{Ar}_{\text{num}}$ cum.% ^b	$^{39}\text{Ar}_{\text{K}}$ /mol	^{38}Ar /mol	cum.%	$^{38}\text{Ar}_{\text{num}}$ /mol	cum.%	$^{38}\text{Ar}_{\text{fam}}$ /mol	cum.%	$^{38}\text{Ar}_{\text{K}}$ /mol	cum.%	$^{38}\text{Ar}_{\text{fam}}$ /mol	cum.%	^{36}Ar /mol	cum.%	$\text{Ar}/\text{Ma} (\pm 2\sigma)$		
Tabor99-15/01																					
1416-02A	0.20	9.47×10^{-15}	16.71	9.37×10^{-13}	42.24	5.07×10^{-16}	4.79	5.60×10^{-16}	39.55	5.55×10^{-16}	42.20	6.21×10^{-19}	4.79	4.51×10^{-18}	4.51	3.17×10^{-15}	42.19	107.5	130.5		
1416-02B	0.25	1.30×10^{-14}	39.68	9.17×10^{-13}	83.58	6.29×10^{-16}	10.72	5.92×10^{-16}	78.00	5.82×10^{-16}	83.50	1.13×10^{-16}	91.53	1.13×10^{-18}	10.73	9.39×10^{-18}	13.91	3.10×10^{-15}	83.52	113.5	112.2
1416-02C	0.30	2.16×10^{-15}	43.51	1.78×10^{-14}	91.61	5.45×10^{-16}	15.87	1.31×10^{-16}	85.93	1.13×10^{-16}	91.53	1.13×10^{-18}	15.89	1.69×10^{-17}	30.85	6.05×10^{-16}	91.57	23.44	24.81		
1416-02D	0.40	5.21×10^{-15}	52.70	7.37×10^{-14}	94.94	1.28×10^{-15}	27.98	7.68×10^{-17}	89.91	4.68×10^{-17}	94.85	8.68×10^{-18}	28.02	2.13×10^{-17}	52.20	2.51×10^{-16}	94.91	23.33	4.38		
1416-02E	0.50	9.43×10^{-15}	69.34	5.18×10^{-14}	97.27	2.79×10^{-15}	54.30	8.48×10^{-17}	94.15	3.28×10^{-17}	97.18	1.29×10^{-17}	54.37	3.91×10^{-17}	83.32	1.77×10^{-16}	97.27	19.38	1.74		
1416-02F	0.60	9.79×10^{-15}	86.62	4.07×10^{-14}	99.10	2.71×10^{-15}	80.03	5.62×10^{-17}	97.83	2.58×10^{-17}	99.01	2.58×10^{-17}	80.14	4.58×10^{-18}	87.91	1.39×10^{-16}	99.12	20.59	1.47		
1416-02G	0.69	5.38×10^{-15}	96.12	1.13×10^{-14}	99.62	1.35×10^{-15}	92.80	2.04×10^{-17}	99.16	7.22×10^{-18}	99.53	7.22×10^{-18}	92.93	5.97×10^{-18}	93.88	4.00×10^{-17}	99.65	22.83	1.72		
1416-02H	0.84	1.44×10^{-15}	98.66	3.15×10^{-16}	99.76	4.75×10^{-16}	97.28	7.21×10^{-18}	99.63	1.99×10^{-18}	99.67	1.99×10^{-18}	97.42	3.21×10^{-17}	97.10	1.28×10^{-17}	99.83	17.61	3.50		
1416-02I	0.99	6.61×10^{-16}	99.83	5.28×10^{-16}	99.78	1.39×10^{-16}	98.60	2.28×10^{-18}	99.78	3.35×10^{-19}	99.69	98.74	1.61×10^{-18}	98.71	4.23×10^{-18}	99.88	28.49	14.10			
1416-02J	2.97	6.81×10^{-16}	100.00	1.32×10^{-15}	100.00	1.58×10^{-16}	100.00	3.71×10^{-18}	100.00	8.38×10^{-19}	100.00	8.38×10^{-19}	100.00	2.04×10^{-18}	100.00	7.79×10^{-18}	100.00	9.23	5.62		
Tabor99-15/02																					
1416-01A	0.20	4.03×10^{-16}	0.41	4.03×10^{-13}	26.67	9.85×10^{-16}	3.26	2.77×10^{-16}	20.72	2.55×10^{-16}	26.65	1.06×10^{-17}	3.26	1.12×10^{-17}	19.74	1.36×10^{-15}	26.59	3.8	28.7		
1416-01B	0.25	7.46×10^{-15}	8.04	6.14×10^{-13}	67.30	7.89×10^{-16}	5.87	3.93×10^{-16}	50.05	3.89×10^{-16}	67.25	8.49×10^{-18}	5.87	4.94×10^{-18}	11.10	2.07×10^{-15}	67.13	59.2	55.6		
1416-01C	0.30	1.20×10^{-15}	9.28	3.01×10^{-13}	87.21	8.36×10^{-16}	8.64	2.07×10^{-16}	65.49	1.91×10^{-16}	87.15	9.01×10^{-18}	8.64	6.96×10^{-18}	23.27	1.02×10^{-15}	87.14	9.0	27.1		
1416-01D	0.40	2.55×10^{-15}	11.89	7.25×10^{-13}	92.01	1.27×10^{-15}	12.85	6.52×10^{-17}	70.35	4.60×10^{-17}	91.94	1.36×10^{-17}	12.84	5.49×10^{-18}	32.87	2.45×10^{-16}	91.93	13.1	4.9		
1416-01E	0.50	9.88×10^{-15}	21.99	3.97×10^{-14}	94.65	3.42×10^{-15}	24.17	6.71×10^{-17}	75.36	2.52×10^{-17}	94.57	3.68×10^{-17}	24.15	5.05×10^{-18}	41.72	1.34×10^{-16}	94.56	18.7	1.2		
1416-01F	0.59	1.99×10^{-14}	42.40	2.96×10^{-14}	96.61	5.93×10^{-15}	43.82	8.97×10^{-17}	82.06	1.88×10^{-17}	96.53	6.39×10^{-17}	43.78	6.97×10^{-18}	53.92	1.01×10^{-16}	96.52	21.7	0.5		
1416-01G	0.74	2.87×10^{-14}	71.75	2.45×10^{-14}	98.23	8.23×10^{-15}	71.06	1.20×10^{-16}	91.01	1.55×10^{-17}	98.16	8.86×10^{-17}	71.01	1.57×10^{-17}	81.47	8.31×10^{-17}	98.14	22.5	0.4		
1416-01H	0.90	1.80×10^{-14}	90.25	1.51×10^{-14}	99.23	5.55×10^{-15}	89.44	7.48×10^{-17}	96.59	9.58×10^{-18}	99.15	9.98×10^{-17}	89.37	5.46×10^{-18}	91.02	1.11×10^{-17}	99.14	21.0	0.5		
1416-01I	1.09	5.18×10^{-15}	95.56	4.69×10^{-15}	99.54	1.58×10^{-15}	94.68	2.32×10^{-17}	98.32	2.97×10^{-18}	99.46	1.70×10^{-17}	94.61	3.21×10^{-18}	96.64	1.58×10^{-17}	99.44	21.2	1.0		
1416-01J	1.28	2.15×10^{-15}	97.77	1.98×10^{-15}	99.67	6.18×10^{-16}	96.73	8.89×10^{-18}	98.99	1.25×10^{-18}	99.60	6.66×10^{-18}	96.66	9.71×10^{-19}	98.34	6.72×10^{-18}	99.58	22.5	2.2		
1416-01K	1.49	8.45×10^{-16}	98.63	1.76×10^{-15}	99.79	3.59×10^{-16}	97.91	5.53×10^{-18}	99.40	1.12×10^{-18}	99.71	3.86×10^{-18}	97.85	5.43×10^{-19}	99.29	5.97×10^{-18}	99.69	15.2	3.3		
1416-01L	3.18	1.33×10^{-15}	100.00	4.09×10^{-15}	100.00	6.51×10^{-16}	100.00	1.00×10^{-17}	100.00	2.59×10^{-18}	100.00	7.01×10^{-18}	100.00	4.05×10^{-19}	100.00	1.38×10^{-17}	100.00	13.3	1.9		
Tabor99-15/03																					
1416-03A	0.20	2.84×10^{-15}	5.23	5.44×10^{-13}	23.78	3.63×10^{-16}	2.69	3.55×10^{-16}	21.93	3.45×10^{-16}	23.83	3.45×10^{-18}	2.74	6.30×10^{-18}	3.99	1.85×10^{-15}	23.92	109.25	112.3		
1416-03B	0.25	1.28×10^{-14}	28.88	1.27×10^{-12}	79.39	7.33×10^{-16}	8.13	8.26×10^{-16}	72.92	8.08×10^{-16}	79.56	8.08×10^{-18}	8.26	9.88×10^{-18}	10.25	4.30×10^{-15}	79.36	103.0	138.6		
1416-03C	0.30	1.38×10^{-15}	31.42	2.29×10^{-13}	89.41	7.34×10^{-16}	13.57	2.48×10^{-16}	82.06	1.45×10^{-16}	89.60	1.45×10^{-17}	13.79	8.78×10^{-17}	24.11	1.02×10^{-17}	72.32	3.52×10^{-16}	93.91	20.05	
1416-03D	0.40	4.78×10^{-15}	40.22	1.03×10^{-13}	93.95	1.36×10^{-15}	23.71	9.21×10^{-17}	87.13	6.59×10^{-17}	94.15	1.59×10^{-17}	41.57	6.18×10^{-18}	76.24	1.66×10^{-16}	96.05	18.34	1.96		
1416-03E	0.50	7.41×10^{-15}	53.85	4.87×10^{-14}	96.08	2.31×10^{-15}	40.89	5.80×10^{-17}	90.72	3.09×10^{-17}	96.29	2.09×10^{-17}	41.73	2.72×10^{-17}	61.70	3.25×10^{-18}	78.30	1.45×10^{-16}	97.92	18.50	
1416-03F	0.59	7.21×10^{-15}	67.12	4.29×10^{-14}	97.95	2.67×10^{-15}	60.69	5.77×10^{-17}	94.28	2.72×10^{-17}	98.16	1.66×10^{-17}	99.31	1.66×10^{-17}	79.92	1.40×10^{-17}	87.20	8.91×10^{-17}	99.07	19.36	
1416-03G	0.69	8.16×10^{-15}	82.13	2.62×10^{-14}	99.10	2.41×10^{-15}	78.60	4.74×10^{-17}	97.21	1.66×10^{-17}	99.38	8.33×10^{-18}	99.89	8.33×10^{-18}	93.10	1.20×10^{-17}	94.82	4.44×10^{-17}	99.64	20.26	
1416-03H	0.84	6.18×10^{-15}	93.49	1.31×10^{-14}	99.67	1.75×10^{-15}	91.56	2.87×10^{-17}	98.98	9.33×10^{-18}	99.00	1.20×10^{-17}	99.18	9.81×10^{-18}	98.51	1.70×10^{-17}	99.86	15.97	1.89		
1416-03I	0.99	2.24×10^{-15}	97.63	5.03×10^{-15}	99.89	8.07×10^{-16}	97.55	1.22×10^{-17}	99.73	3.19×10^{-18}	100.11	3.19×10^{-18}	100.00	1.52×10^{-18}	100.00	2.35×10^{-18}	100.00	8.43×10^{-18}	100.00	4.50	

a) $J = 0.003193 \pm 0.0000018$; b) cum. %, cumulative percentage.

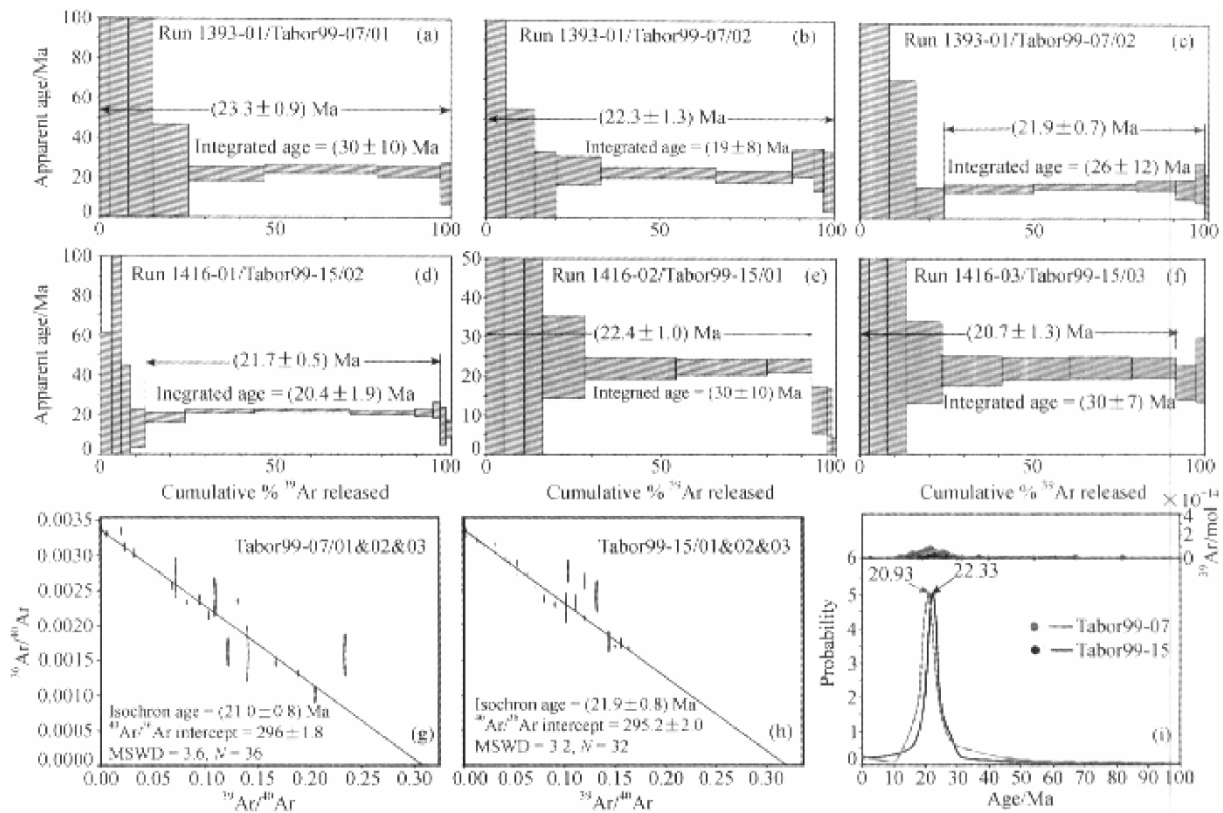


Fig. 4. Apparent age spectra ((a)–(f)), the isotope correlation diagrams ((g)–(h)), and the ideograms (i) of the hollandite and cryptomelane samples.

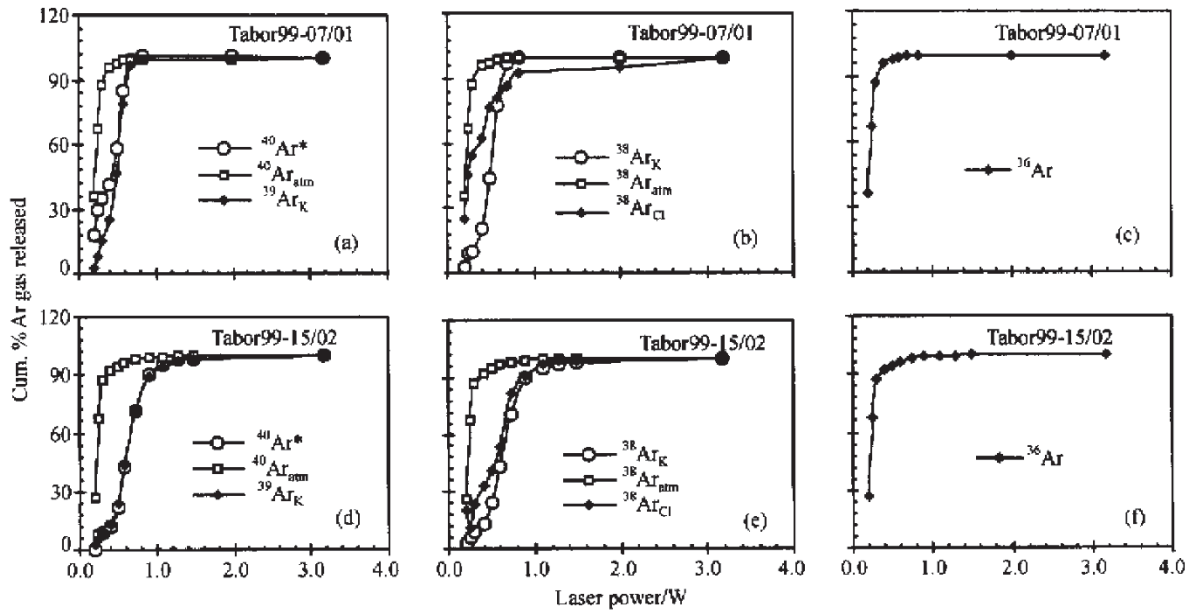


Fig. 5. Cumulative percentage of various Ar isotopes released versus the laser power values.

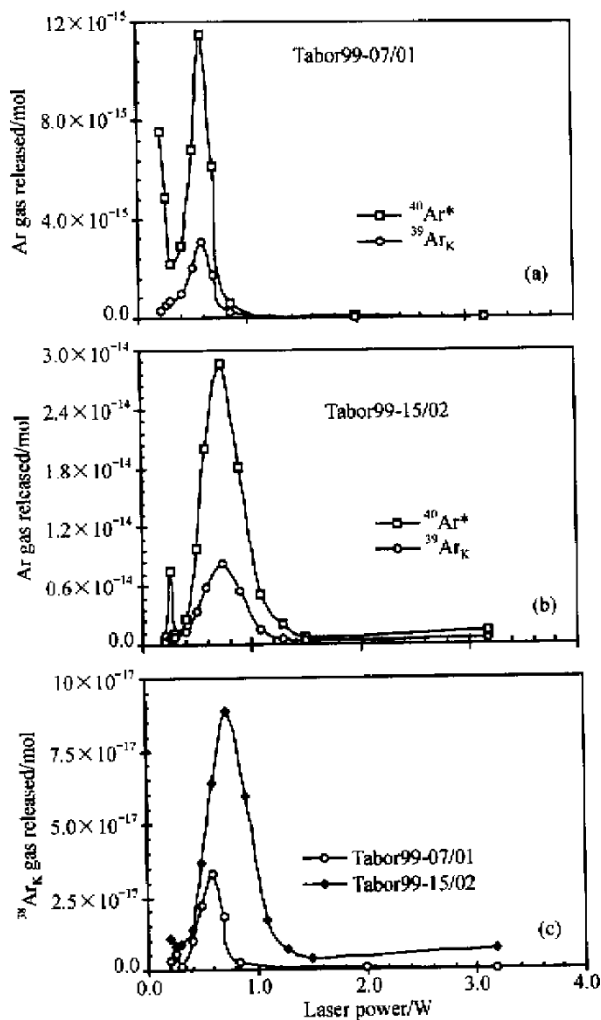


Fig. 6. Degassing curves of ⁴⁰Ar*, ³⁹Ar_K, and ³⁸Ar_K showing the compatibility of these radiogenic and nucleogenic isotopes.

at 0.20 W), and there is a striking increase in the release of this isotope before the laser power (P) reached 0.4 W (fig. 5(a), (d)). Very little gas was obtained at the heating steps while the laser power is higher than 0.4 W.

The degassing pattern of the radiogenic ⁴⁰Ar (⁴⁰Ar*) is very distinct from that of the ⁴⁰Ar_{atm}, beginning to release slowly from the sample at $P = 0.3$ W. However, ~18% ⁴⁰Ar* was released from the sample Tabor99-07/01 upon heating, presumably caused by its low crystallinity relative to the sample Tabor99-05/02, as observed by SEM study. At approximate 0.4 W, there is a marked increase in ⁴⁰Ar* release, and more than 99% and 90% ⁴⁰Ar* were degassed in the subsequent three steps where the laser power reached 0.84 and 0.90 W for the two samples, respectively (fig. 5(a), (d)), indicating that the sites hosting ⁴⁰Ar* become open to Ar degassing. The

³⁹Ar_K degassing behavior is extremely similar to the degassing history of ⁴⁰Ar* (fig. 5(a), (d), fig. 6(a)–(b)), indicating that the two isotopes occupy the same or equivalent mineral sites.

The isotope ³⁸Ar consists of three distinct components, i.e. ³⁸Ar_{atm}, ³⁸Ar_K, and ³⁸Ar_{Cl}. ³⁸Ar_{atm} is estimated assuming a ⁴⁰Ar_{atm}/³⁸Ar_{atm} ratio of 1575.9^[5]. ³⁸Ar_K (nucleogenic ³⁸Ar generated by reaction on K during neutron irradiation) is calculated using a correction factor (³⁹Ar_K/³⁸Ar_K = 0.01077) for the generation of ³⁸Ar in the reactor. ³⁸Ar_{Cl} (nucleogenic ³⁸Ar generated by reaction on Cl) is estimated by difference. The degassing profiles of ³⁸Ar for the two samples (fig. 5(b), (e)), suggest two distinct reservoirs hosting the isotopes of different origins. The first reservoir is easily degassed at $P < 0.3$ W (more than 90% ³⁸Ar_{atm} was released in present case), and it hosts primarily ³⁸Ar_{atm}. The second reservoir releases its significant amounts of ³⁸Ar gas fraction at $P > 0.3$ W, and it hosts predominantly ³⁸Ar_K and ³⁸Ar_{Cl}. It appears that the release of ³⁸Ar_K requires a laser power slightly higher than that does ³⁸Ar_{Cl}.

The degassing pattern of ³⁶Ar mimics the ⁴⁰Ar_{atm} release curves (fig. 5(c), (f)), indicating the close behavior between these isotopes, and confirming that ³⁶Ar is essentially atmospheric.

4 Discussion

The diffusion and retentivity of K and Ar within the hollandite-group minerals has been a matter of long debated. Sreenivas and Roy^[19] proposed that the large tunnel structure, *A* site disordering, and partial occupancy of the tunnel sites lead to low activation energies for the *A* cations, resulting in a high cation-exchange capacity for these minerals. According to these authors, high cation exchange would also imply potential loss of K and radiogenic ⁴⁰Ar*. On the other hand, Vicat et al.^[20] observed a superstructure along the *c* axis in synthetic hollandite that he interpreted as one-dimensional ordering of K cations in the partially filled *A* sites, following the sequences K-K-□-K-K-□. Ordering of the *A* cations indicates restricted mobility of the cations along the tunnel direction, an important characteristic for the K and Ar retentivity of hollandite and cryptomelane. Restricted mobility of *A* cations has also been noticed by Sinclair et al.^[21] who identified the presence of square-shaped bottlenecks along the channels. These bottlenecks restrict cation motion and account for the high resistance to leaching presented by hollandite type structures^[21].

Well-developed plateau ages and the internal concordance between the plateau, integrated, isochron, and ideogram ages (fig. 4) imply the fact that the cation ex-

changes in the tunnel sites (*A*-site) has been very minor during the geological history of the samples currently investigated. In the other words, the results indicate that supergene Mn oxides in this study host their radiogenic and nucleogenic gas fractions in a tight crystallographic reservoir (i.e. the tunnel sites) that has been closed since these oxide minerals were precipitated from weathering solutions. This has been further supported by the argon isotope release patterns (fig. 5). The large uncertainties of apparent ages in the first steps (fig. 4(a)–(f)) resulted from the overwhelming amounts of atmospheric ^{40}Ar that significantly dilutes the relatively smaller radiogenic and nucleogenic Ar fractions (table 1). More than 90% of this atmospheric component was released in the first three steps ($P < 0.3$ W), suggesting that the $^{40}\text{Ar}_{\text{atm}}$ is either hosted in less retentive intercrystalline sites (fig. 1) in the mineral structures or adsorbed onto the crystal surfaces, a scenario evidenced by previous mineralogical and textural work^[22]. The $^{40}\text{Ar}/^{36}\text{Ar}$ ratios ~ 295 (fig. 4(g)–(h)) substantiate that (1) both the hollandite and cryptomelane do not host excess argon; and (2) isotopic exchange has not occurred since the minerals were exposed to the meteoric waters and the Earth's surface.

A notorious problem in dating very-fined minerals using $^{40}\text{Ar}/^{39}\text{Ar}$ method is the loss or redistribution of $^{39}\text{Ar}_K$ by recoil in the reactor or in the subsequent bake-out procedure preceding the isotopic analysis^[5,6,12,23,24]. The recoiled $^{39}\text{Ar}_K$ displaced from its original crystal sites may be completely lost to the surrounding atmosphere, loosely lodged in poorly retentive intercrystalline or damaged sites, or reimplanted/trapped into other intracrystalline sites in the mineral structures. If recoil occurred, and if the recoiled $^{39}\text{Ar}_K$ were completely escaped out of the mineral structure, the initial heating steps would yield erroneously old apparent ages, and the subsequent higher power steps should give rise to younger ages than the initial degassing steps^[24]. In this case, the integrated ages are expected to be older than the corresponding plateaus. If the recoiled ^{39}Ar was reimplanted or trapped into less retentive sites (presumably the intercrystalline sites illustrated in fig. 1), the initial steps, although mostly atmospheric, contain radiogenic $^{40}\text{Ar}^*$ and recoiled ^{39}Ar easily released from their implantation or trapping sites. An apparent age younger than the true age would be expected. With progressively increasing level of the laser power, $^{40}\text{Ar}^*$ is released from sites that has lost ^{39}Ar by recoil, and apparent ages older than the true age for the sample will be obtained. At higher power values, the retentive sites not subject to recoil loss and hosting significant amounts of $^{40}\text{Ar}^*$ and ^{39}Ar are degassed, a plateau age representing the true mineral age is obtained. How-

ever, this is not the case for our samples: well-behaved degassing steps that plot on a plateau, and the concordance of plateau ages with the respective isochron ages, suggest no $^{39}\text{Ar}_K$ is lost by recoil. Absence of recoil has also been demonstrated by the excellent match between the degassing behaviors of $^{40}\text{Ar}^*$ and $^{39}\text{Ar}_K$ (fig. 5(b), (e), fig. 6(a)–(b)). The only difference in radiogenic and nucleogenic Ar release between Tabor99-07/01 and Tabor99-15/02 is the released amounts of these two components: the later released more $^{40}\text{Ar}^*$ and $^{39}\text{Ar}_K$ than the former (fig. 6). This has resulted from the higher K concentration in the Tabor99-15/02 sample (fig. 3(a), (c)). Although the cumulative curves of % Ar gas released for $^{40}\text{Ar}^*$ and $^{39}\text{Ar}_K$ are essentially similar, it is true that both samples released more $^{40}\text{Ar}^*$ in the first three (Tabor99-07/01) or two (Tabor99-15/02) steps than the subsequent step(s), forming a valley and peak in the left parts of the curves, respectively (fig. 6(a), (b)). We interpret this phenomenon as the occurrence of $^{40}\text{Ar}^*$ in some less retentive reservoirs relative to the tunnel sites, such as the intercrystalline sites, porous spaces, and crystal defects.

The atmospheric ^{38}Ar and ^{36}Ar behaved very similarly to $^{40}\text{Ar}_{\text{atm}}$ (fig. 5), confirmed by the close degassing patterns of these isotopes, and indicating that ^{36}Ar is essentially atmospheric, and that they are primarily hosted by less retentive crystal sites or adsorbed onto the crystal surface. $^{38}\text{Ar}_K$ and $^{38}\text{Ar}_{\text{Cl}}$ mimic $^{40}\text{Ar}^*$ as well as $^{39}\text{Ar}_K$, but $^{38}\text{Ar}_K$ seems the most retentive compared to other radiogenic and nucleogenic isotopes (fig. 5(b), (e)): the cause for this discrepancy is still undetermined, and worthy to be examined in the future studies.

Another discrepancy between these two samples is that Tabor99-15/02 sample requires higher laser power level for the same cumulative percentage of argon gas released (figs. 5 and 6). This has been possibly caused by the higher crystallinity of the cryptomelane minerals in this sample, as evidenced by petrographic and SEM observations.

5 Conclusions

Well-defined and reproducible apparent ages, and the consistence of plateau with the respective integrated and isochron ages, confirm that $^{40}\text{Ar}/^{39}\text{Ar}$ method is a promising approach in dating supergene manganese oxides. $^{40}\text{Ar}/^{36}\text{Ar}$ ratios ~ 295 indicate that neither excess Ar nor Ar/K loss has occurred during the sample history. The samples release little radiogenic and nucleogenic Ar at the low range of laser power (0.2–0.4 W). The high power release of $^{40}\text{Ar}^*$, $^{39}\text{Ar}_K$, $^{38}\text{Ar}_K$ and $^{38}\text{Ar}_{\text{Cl}}$, is likely correlated to the degassing of very tight crystalline reservoirs (i.e. tunnel sites). Tiny gas fraction obtained by the high-

est power level (>1.0 W) is related to the collapse of tunnel sites^[13].

This study tells the specific range of laser power (0.4—1.0 W) most favorable for efficient separation of atmospheric Ar isotopes from the radiogenic and nucleogenic compartments, and thus for the extraction of meaningful geochronological information useful in our understanding in the formation and evolution of weathering profiles. However, the design of laser power level during the isotopic analysis may be subjected to variation with the crystallinity, the crystal size, and the K contents of specific samples.

Acknowledgements We are indebted to D. Franks, M. Conroy, and Y. Feng for their assistance in the field and laboratory. Thanks are also due to the Center for Microscopy and Microanalysis at The University of Queensland for allowing the senior author to access various facilities. Review and comments by anonymous referees are acknowledged. This study was supported by the National Key Research Project of China (Grant No. G1999043207-3) and ARC of Australia (Grant Nos. A39531815 and A39701507).

References

1. Bird, M. I., Chivas, A. R., Oxygen isotope dating of the Australian regolith, *Nature*, 1988, 331: 513.
2. Schmidt, P. W., Embleton, B. J. J., Paleomagnetic results from sediments of the Perth Basin, Western Australia, and their bearing on the timing of regional lateritization, *Palaeogeog., Paleoclimat., Palaeoecol.*, 1976, 19: 257.
3. Pavich, M. J., Brown, L., Valette, S. J. N. et al., ¹⁰Be analysis of a Quaternary weathering profile in the Virginia Piedmont, *Geology*, 1985, 13: 39.
4. Halliday, A. N., ⁴⁰Ar/³⁹Ar step heating studies of clay concentrates from the Irish orebodies, *Geochim. Cosmochim. Acta*, 1978, 42: 1851.
5. McDougall, I., Harrison, T. M., Geochronology and thermochronology by the ⁴⁰Ar/³⁹Ar method, Oxford: Oxford University Press, 1988, 1—292.
6. Vasconcelos, P. M., Becker, T. A., Renne, P. R. et al., Age and duration of weathering by ⁴⁰Ar/³⁹Ar analysis of potassium-manganese oxides, *Science*, 1992, 258: 451.
7. Lo, C. H., Lee, J. K. W., Onstott, T. C., Argon release mechanisms of biotite in vacuo and the role of short-circuit diffusion and recoil, *Chem. Geol.*, 2000, 165: 135.
8. Yashvili, L. P., Gukasyan, R. K., Use of cryptomelane for K-Ar dating of manganese ores of the Sevkar-Sariguyukh deposit, Armenia, *Doklady Akademii Nauk SSSR, Earth-Science Section*, 1973, 212: 185.
9. Idnurm, M., Paleomagnetic dating of weathered profiles, 12th International Sedimentological Congress, Canberra: Highland Press, 1986, 46—53.
10. Burns, R., Burns, V. M., Manganese oxides, *Marine Minerals* (ed. Ribbe, P. H.), Washington: Mineralogical Society of America, 1979, 6: 1.
11. Byröm, A., Byröm, A. M., The crystall structure of Hollandite, the related manganese oxide minerals, and α -MnO₂, *Acta Crystal*, 1950, 3: 146.
12. Vasconcelos, P. M., Renne, P. R., Brimhall, G. H. et al., Direct dating of weathering phenomena by ⁴⁰Ar/³⁹Ar and K-Ar analysis of supergene K-Mn oxides, *Geochim. Cosmochim. Acta*, 1994, 58: 1635.
13. Vasconcelos, P. M., Renne, P. R., Becker, T. A. et al., Mechanisms and kinetics of atmospheric, radiogenic, and nucleogenic argon release from cryptomelane during ⁴⁰Ar/³⁹Ar analysis, *Geochim. Cosmochim. Acta*, 1995, 59: 2057.
14. Dammer, D., Chivas, A. R., McDougall, I., Isotopic dating of supergene manganese oxides from the Groote Eylandt deposit, Northern Territory, Australia, *Econ. Geol.*, 1996, 91: 386.
15. Ruffet, G., Innocent, C., Michard, A. et al., A geochronological ⁴⁰Ar/³⁹Ar and ⁸⁷Rb/⁸⁷Sr study of K-Mn oxides from the weathering sequence of Azul, Brazil, *Geochim. Cosmochim. Acta*, 1996, 60: 2219.
16. Hénocque, O., Ruffet, G., Colin, F. et al., ⁴⁰Ar/³⁹Ar dating of West African lateritic cryptomelanes, *Geochim. Cosmochim. Acta*, 1998, 62: 2739.
17. Li, J. W., Vasconcelos, P. M., Cenozoic continental weathering and its implications for paleoclimate: evidence from ⁴⁰Ar/³⁹Ar geochronology of supergene K-Mn oxides in Mt. Tabor, central Queensland, Australia, *Earth Planet. Sci. Lett.*, 2002, 200: 223.
18. Renne, P. R., Swisher, C. C., Deino, A. L. et al., Intercalibration of standards, absolute ages and uncertainties in ⁴⁰Ar/³⁹Ar dating, *Chem. Geol.*, 1998, 145: 117.
19. Sreenivas, B. L., Roy, R., Observations on cation exchange in some manganese minerals by electrodialysis, *Econ. Geol.*, 1961, 56: 198.
20. Vicat, J., Fanchon, E., Strobel, P. et al., The structure of K_{1.33}Mn₈O₁₆ and cation ordering in hollandite-type structures, *Acta Crystallograph.*, 1986, B42: 162.
21. Sinclair, W., McLaughlin, G. M., Rinwood, A. E., The structure and chemistry of a barium titanate hollandite-type phase, *Acta Crystallograph.*, 1980, B36: 2913.
22. McKenzie, R. M., Manganese oxides and hydroxides (eds. Dixon, J. B., Weed S. B.), *Minerals in Soil Environments*, Wisconsin: Soil Science Society of America, 1989, 439—465.
23. Turner, G., Cadogan, P. H., Possible effects of ³⁹Ar recoil in ⁴⁰Ar/³⁹Ar dating, *Geochim. Cosmochim. Acta*, 1974, 2: 1601.
24. Hunkele, J. C., Smith, S. P., The realities of recoil: ³⁹Ar recoil out of small grains and anomalous age patterns in ³⁹Ar/⁴⁰Ar dating, *Geochim. Cosmochim. Acta*, 1976 (Suppl. 7): 1987.

(Received January 15, 2002; accepted April 19, 2002)

Table 1 Results of $^{40}\text{Ar}/^{39}\text{Ar}$ laser incremental heating analysis^{a)}

Run ID#	Power /W	$^{40}\text{Ar}^*$ /mol	$^{40}\text{Ar}^*$ cum.% ^{b)}	$^{40}\text{Ar}_{\text{lam}}$ /mol	$^{40}\text{Ar}_{\text{lam}}$ cum.% ^{b)}	$^{39}\text{Ar}_{\text{K}}$ /mol	$^{39}\text{Ar}_{\text{K}}$ cum.% ^{b)}	^{38}Ar /mol	^{38}Ar cum.% ^{b)}	$^{38}\text{Ar}_{\text{lam}}$ /mol	$^{38}\text{Ar}_{\text{lam}}$ cum.% ^{b)}	$^{38}\text{Ar}_{\text{K}}$ /mol	$^{38}\text{Ar}_{\text{K}}$ cum.% ^{b)}	$^{38}\text{Ar}_{\text{CI}}$ /mol	$^{38}\text{Ar}_{\text{CI}}$ cum.% ^{b)}	^{36}Ar /mol	^{36}Ar cum.% ^{b)}	$\Delta \text{ge}/\text{Ma} (\pm 2\sigma)$	
Tabor99-07/01 ^{c)}																			
1393-01A	0.20	7.54×10^{-15}	17.90	6.20×10^{-13}	35.83	2.71×10^{-16}	2.85	4.04×10^{-6}	32.84	3.93×10^{-16}	35.74	2.92×10^{-18}	3.03	7.35×10^{-18}	24.68	2.09×10^{-15}	35.89	175.5	248.7
1393-01B	0.25	4.87×10^{-15}	29.47	5.36×10^{-13}	66.79	5.11×10^{-16}	8.21	3.52×10^{-6}	61.44	3.40×10^{-16}	66.61	5.50×10^{-18}	8.72	6.61×10^{-17}	45.48	1.81×10^{-15}	66.92	59.5	99.5
1393-01C	0.30	2.16×10^{-15}	34.61	3.58×10^{-13}	87.49	6.78×10^{-16}	15.32	2.31×10^{-6}	80.25	2.27×10^{-16}	87.26	1.30×10^{-18}	10.07	2.86×10^{-18}	54.48	1.21×10^{-15}	87.65	20.9	45.6
1393-01D	0.40	2.93×10^{-15}	41.62	1.44×10^{-13}	95.84	9.51×10^{-16}	25.29	1.04×10^{-6}	88.73	9.18×10^{-17}	95.59	1.02×10^{-17}	20.66	2.44×10^{-18}	62.17	4.89×10^{-16}	96.02	20.2	13.3
1393-01E	0.50	6.84×10^{-15}	57.87	2.89×10^{-14}	97.52	2.03×10^{-15}	46.66	4.50×10^{-7}	92.38	1.83×10^{-17}	97.26	2.19×10^{-17}	43.37	4.66×10^{-18}	76.83	9.82×10^{-17}	97.70	21.7	1.7
1393-01F	0.59	1.15×10^{-14}	85.11	2.52×10^{-14}	98.98	3.05×10^{-15}	78.73	5.02×10^{-17}	96.46	1.60×10^{-17}	98.71	3.29×10^{-17}	77.43	1.26×10^{-18}	80.79	8.55×10^{-17}	99.16	24.2	1.0
1393-01G	0.69	6.18×10^{-15}	99.78	1.06×10^{-14}	99.59	1.73×10^{-15}	96.87	2.72×10^{-17}	98.67	6.75×10^{-18}	99.33	1.86×10^{-17}	96.71	1.79×10^{-18}	86.44	3.60×10^{-17}	99.78	23.0	1.2
1393-01H	0.84	6.19×10^{-16}	101.25	1.52×10^{-15}	99.68	2.34×10^{-16}	99.33	5.31×10^{-18}	99.10	9.67×10^{-19}	99.41	2.52×10^{-18}	99.31	1.82×10^{-18}	92.18	5.16×10^{-18}	99.87	17.1	5.1
1393-01I	1.99	4.19×10^{-17}	101.35	4.18×10^{-16}	99.70	3.26×10^{-17}	99.67	1.59×10^{-18}	99.23	2.65×10^{-19}	99.44	3.52×10^{-19}	99.68	9.78×10^{-19}	95.26	1.41×10^{-18}	99.89	8.3	43.2
1393-01J	3.18	-6.12×10^{-16}	100.00	1.24×10^{-15}	100.00	2.60×10^{-17}	100.00	2.54×10^{-18}	99.44	7.89×10^{-19}	100.00	2.80×10^{-19}	100.00	1.47×10^{-18}	100.00	4.21×10^{-18}	100.00	-159.2	57.5
Tabor99-07/02																			
1393-02A	0.20	9.91×10^{-16}	4.16	4.94×10^{-13}	54.88	4.09×10^{-16}	5.88	3.18×10^{-16}	48.78	3.13×10^{-16}	54.90	3.13×10^{-18}	5.88	1.41×10^{-18}	1.36	1.67×10^{-15}	54.26	16.94	90.27
1393-02B	0.25	2.98×10^{-17}	4.29	2.98×10^{-14}	88.01	5.59×10^{-16}	13.91	1.95×10^{-6}	78.83	1.89×10^{-16}	88.05	1.89×10^{-18}	13.90	4.74×10^{-18}	5.93	1.03×10^{-15}	87.73	14.86	52.30
1393-02C	0.30	1.07×10^{-15}	8.80	5.01×10^{-14}	93.57	4.35×10^{-16}	20.15	4.98×10^{-17}	84.94	1.17×10^{-17}	93.61	9.17×10^{-18}	20.14	2.89×10^{-17}	33.70	1.72×10^{-16}	93.34	14.17	12.51
1393-02D	0.40	3.47×10^{-15}	23.41	1.86×10^{-14}	95.65	8.92×10^{-16}	32.95	5.06×10^{-17}	88.10	1.01×10^{-17}	95.69	1.18×10^{-17}	32.94	2.86×10^{-17}	61.22	6.42×10^{-17}	95.43	22.35	3.47
1393-02E	0.50	8.20×10^{-15}	58.25	2.47×10^{-14}	98.40	2.29×10^{-15}	65.80	4.10×10^{-17}	94.39	1.57×10^{-18}	98.44	1.57×10^{-17}	65.77	2.37×10^{-17}	84.06	8.50×10^{-17}	98.19	20.74	1.39
1393-02F	0.59	5.23×10^{-15}	80.26	1.11×10^{-14}	99.63	1.55×10^{-15}	87.98	2.55×10^{-17}	98.31	7.03×10^{-18}	99.67	7.03×10^{-18}	87.94	1.44×10^{-17}	95.10	3.89×10^{-17}	99.46	19.43	1.54
1393-02G	0.69	2.12×10^{-15}	89.18	1.27×10^{-15}	99.77	4.14×10^{-16}	93.93	5.89×10^{-18}	99.21	8.08×10^{-19}	99.81	8.08×10^{-19}	93.89	4.27×10^{-18}	98.21	5.55×10^{-18}	99.64	29.51	4.14
1393-02H	0.85	1.21×10^{-15}	94.27	3.14×10^{-16}	99.80	2.14×10^{-16}	97.01	1.31×10^{-18}	99.41	1.99×10^{-19}	99.84	1.99×10^{-19}	96.97	9.19×10^{-19}	99.10	2.45×10^{-18}	99.72	32.77	8.49
1393-02I	3.18	1.38×10^{-15}	100.00	1.45×10^{-16}	100.00	2.06×10^{-16}	99.98	8.82×10^{-19}	100.00	6.23×10^{-19}	100.00	1.23×10^{-19}	100.00	1.24×10^{-19}	100.00	7.70×10^{-18}	100.00	39.44	9.08
Tabor99-07/03																			
1393-03A	0.20	3.96×10^{-15}	15.97	9.87×10^{-13}	85.10	6.28×10^{-16}	8.12	6.30×10^{-16}	77.41	6.26×10^{-16}	85.11	6.26×10^{-19}	8.13	3.86×10^{-18}	5.85	3.34×10^{-15}	85.22	37.46	126.5
1393-03B	0.25	3.30×10^{-15}	29.28	1.19×10^{-14}	95.36	5.94×10^{-16}	15.80	8.02×10^{-17}	87.26	7.55×10^{-17}	95.37	7.55×10^{-19}	15.81	3.95×10^{-18}	11.82	4.06×10^{-16}	95.60	32.23	16.33
1393-03C	0.30	3.64×10^{-16}	30.75	3.00×10^{-14}	97.95	6.17×10^{-16}	23.78	2.66×10^{-17}	90.53	1.90×10^{-17}	97.96	1.90×10^{-18}	23.80	5.70×10^{-18}	20.45	1.02×10^{-16}	98.21	3.27	5.32
1393-03D	0.40	4.62×10^{-15}	49.38	1.05×10^{-14}	98.86	1.99×10^{-15}	49.54	2.84×10^{-17}	94.02	6.68×10^{-18}	98.87	6.68×10^{-18}	49.57	1.50×10^{-17}	43.22	3.58×10^{-17}	99.13	17.30	1.12
1393-03E	0.50	7.56×10^{-15}	79.85	5.89×10^{-15}	99.37	2.25×10^{-15}	78.70	3.01×10^{-17}	97.71	3.73×10^{-18}	99.38	3.73×10^{-18}	78.76	2.26×10^{-17}	77.45	1.99×10^{-17}	99.63	19.19	0.72
1393-03F	0.59	3.01×10^{-15}	92.00	1.30×10^{-15}	99.48	8.89×10^{-16}	90.20	9.77×10^{-18}	98.91	8.28×10^{-19}	99.49	8.28×10^{-19}	90.26	8.12×10^{-18}	89.73	4.42×10^{-18}	99.75	19.41	1.15
1393-03G	0.69	9.85×10^{-16}	95.98	8.70×10^{-16}	99.56	4.35×10^{-16}	95.82	4.76×10^{-18}	99.50	5.52×10^{-19}	99.57	5.52×10^{-19}	95.89	3.66×10^{-18}	95.28	2.94×10^{-18}	99.82	16.99	2.28
1393-03H	0.84	6.09×10^{-16}	98.43	2.98×10^{-16}	99.58	2.21×10^{-16}	98.68	2.51×10^{-18}	99.80	1.89×10^{-19}	99.59	1.89×10^{-19}	98.75	2.13×10^{-18}	98.52	1.01×10^{-18}	99.85	15.81	4.41
1393-03I	3.18	3.19×10^{-16}	100.00	4.41×10^{-15}	100.00	1.01×10^{-16}	100.00	1.42×10^{-18}	100.00	1.79×10^{-19}	100.00	2.79×10^{-19}	100.00	9.63×10^{-19}	100.00	2.61×10^{-18}	100.00	12.36	9.56

(To be continued on the next page)

(Continued)

Run ID#	Power /W	⁴⁰ Ar*	⁴⁰ Ar [*] cum. % ^a	⁴⁰ Ar _{aim}	⁴⁰ Ar _{aim} cum. % ^b	³⁹ Ar _K	³⁹ Ar _K cum. % _b	³⁸ Ar	³⁸ Ar cum. % _b	³⁸ Ar _{aim}	³⁸ Ar _{aim} cum. % _b	³⁸ Ar _K	³⁸ Ar _K cum. % _b	³⁶ ArCl	³⁶ ArCl cum. % _b	³⁶ Ar/mol	³⁶ Ar cum. %/Ma (±2σ)	
Tabor99-15/01																		
1416-02A	0.20	9.47×10 ⁻¹⁵	16.71	9.37×10 ⁻¹³	42.24	5.07×10 ⁻¹⁶	4.79	5.60×10 ⁻¹⁶	39.55	5.55×10 ⁻¹⁶	42.20	6.21×10 ⁻¹⁹	4.79	4.51×10 ⁻¹⁸	4.51	3.17×10 ⁻¹⁵	42.19	107.5 130.5
1416-02B	0.25	1.30×10 ⁻¹⁴	39.68	9.17×10 ⁻¹³	83.58	6.29×10 ⁻¹⁶	10.72	5.92×10 ⁻¹⁶	78.00	5.82×10 ⁻¹⁶	83.50	5.82×10 ⁻¹⁹	10.73	9.39×10 ⁻¹⁸	13.91	3.10×10 ⁻¹⁵	83.52	113.5 112.2
1416-02C	0.30	2.16×10 ⁻¹⁵	43.51	1.78×10 ⁻¹⁴	91.61	5.45×10 ⁻¹⁶	15.87	1.31×10 ⁻¹⁶	85.93	1.13×10 ⁻¹⁶	91.53	1.13×10 ⁻¹⁸	15.89	1.69×10 ⁻¹⁷	30.85	6.05×10 ⁻¹⁶	91.57	23.44 24.81
1416-02D	0.40	5.21×10 ⁻¹⁵	52.70	7.37×10 ⁻¹⁴	94.94	1.28×10 ⁻¹⁵	27.98	7.68×10 ⁻¹⁷	89.91	4.68×10 ⁻¹⁷	94.85	8.68×10 ⁻¹⁸	28.02	2.13×10 ⁻¹⁷	52.20	2.51×10 ⁻¹⁶	94.91	23.33 4.38
1416-02E	0.50	9.43×10 ⁻¹⁵	69.34	5.18×10 ⁻¹⁴	97.27	2.79×10 ⁻¹⁵	54.30	8.48×10 ⁻¹⁷	94.15	3.28×10 ⁻¹⁷	97.18	1.29×10 ⁻¹⁷	54.37	3.91×10 ⁻¹⁷	83.32	1.77×10 ⁻¹⁶	97.27	19.38 1.74
1416-02F	0.60	9.79×10 ⁻¹⁵	86.62	4.07×10 ⁻¹⁴	99.10	2.71×10 ⁻¹⁵	80.03	5.62×10 ⁻¹⁷	97.83	2.58×10 ⁻¹⁷	99.01	2.58×10 ⁻¹⁷	80.14	4.58×10 ⁻¹⁸	87.91	1.39×10 ⁻¹⁶	99.12	20.59 1.47
1416-02G	0.69	5.38×10 ⁻¹⁵	96.12	1.13×10 ⁻¹⁴	99.62	1.35×10 ⁻¹⁵	92.80	2.04×10 ⁻¹⁷	99.16	7.22×10 ⁻¹⁸	99.53	7.22×10 ⁻¹⁸	92.93	5.97×10 ⁻¹⁸	93.88	4.00×10 ⁻¹⁷	99.65	22.83 1.72
1416-02H	0.84	1.44×10 ⁻¹⁵	98.66	3.15×10 ⁻¹⁶	99.76	4.75×10 ⁻¹⁶	97.28	7.21×10 ⁻¹⁸	99.63	1.99×10 ⁻¹⁸	99.67	1.99×10 ⁻¹⁸	97.42	3.21×10 ⁻¹⁸	97.10	1.28×10 ⁻¹⁷	99.83	17.61 3.50
1416-02I	0.99	6.61×10 ⁻¹⁶	99.83	5.28×10 ⁻¹⁶	99.78	1.39×10 ⁻¹⁶	98.60	2.28×10 ⁻¹⁸	99.78	3.35×10 ⁻¹⁹	99.69	3.35×10 ⁻¹⁹	98.74	1.61×10 ⁻¹⁸	98.71	4.23×10 ⁻¹⁸	99.88	28.49 14.10
1416-02J	2.97	6.81×10 ⁻¹⁶	100.00	1.32×10 ⁻¹⁵	100.00	1.58×10 ⁻¹⁶	100.00	3.71×10 ⁻¹⁸	100.00	8.38×10 ⁻¹⁹	100.00	8.38×10 ⁻¹⁹	100.00	2.04×10 ⁻¹⁸	100.00	7.79×10 ⁻¹⁸	100.00	9.23 5.62
Tabor99-15/02																		
1416-01A	0.20	4.03×10 ⁻¹⁶	0.41	4.03×10 ⁻¹³	26.67	9.85×10 ⁻¹⁶	3.26	2.77×10 ⁻¹⁶	20.72	2.55×10 ⁻¹⁶	26.65	1.06×10 ⁻¹⁷	3.26	1.12×10 ⁻¹⁷	19.74	1.36×10 ⁻¹⁵	26.59	3.8 28.7
1416-01B	0.25	7.46×10 ⁻¹⁵	8.04	6.14×10 ⁻¹³	67.30	7.89×10 ⁻¹⁶	5.87	3.93×10 ⁻¹⁶	50.05	3.89×10 ⁻¹⁶	67.25	8.49×10 ⁻¹⁸	5.87	4.94×10 ⁻¹⁸	11.10	2.07×10 ⁻¹⁵	67.13	59.2 55.6
1416-01C	0.30	1.20×10 ⁻¹⁵	9.28	3.01×10 ⁻¹³	87.21	8.36×10 ⁻¹⁶	8.64	2.07×10 ⁻¹⁶	65.49	1.91×10 ⁻¹⁶	87.15	9.01×10 ⁻¹⁸	8.64	6.96×10 ⁻¹⁸	23.27	1.02×10 ⁻¹⁵	87.14	9.0 27.1
1416-01D	0.40	2.55×10 ⁻¹⁵	11.89	7.25×10 ⁻¹³	92.01	1.27×10 ⁻¹⁵	12.85	6.52×10 ⁻¹⁷	70.35	4.60×10 ⁻¹⁷	91.94	1.36×10 ⁻¹⁷	12.84	5.49×10 ⁻¹⁸	32.87	2.45×10 ⁻¹⁶	91.93	13.1 4.9
1416-01E	0.50	9.88×10 ⁻¹⁵	21.99	3.97×10 ⁻¹⁴	94.65	3.42×10 ⁻¹⁵	24.17	6.71×10 ⁻¹⁷	75.36	2.52×10 ⁻¹⁷	94.57	3.68×10 ⁻¹⁷	24.15	5.05×10 ⁻¹⁸	41.72	1.34×10 ⁻¹⁶	94.56	18.7 1.2
1416-01F	0.59	1.99×10 ⁻¹⁴	42.40	2.96×10 ⁻¹⁴	96.61	5.93×10 ⁻¹⁵	43.82	8.97×10 ⁻¹⁷	82.06	1.88×10 ⁻¹⁷	96.53	6.39×10 ⁻¹⁷	43.78	6.97×10 ⁻¹⁸	53.92	1.01×10 ⁻¹⁶	96.52	21.7 0.5
1416-01G	0.74	2.87×10 ⁻¹⁴	71.75	2.45×10 ⁻¹⁴	98.23	8.23×10 ⁻¹⁵	71.06	1.20×10 ⁻¹⁶	91.01	1.55×10 ⁻¹⁷	98.16	8.86×10 ⁻¹⁷	71.01	1.57×10 ⁻¹⁷	81.47	8.31×10 ⁻¹⁷	98.14	22.5 0.4
1416-01H	0.90	1.80×10 ⁻¹⁴	90.25	1.51×10 ⁻¹⁴	99.23	5.55×10 ⁻¹⁵	89.44	7.48×10 ⁻¹⁷	96.59	9.58×10 ⁻¹⁸	99.15	5.98×10 ⁻¹⁷	89.37	5.46×10 ⁻¹⁸	91.02	5.11×10 ⁻¹⁷	99.14	21.0 0.5
1416-01I	1.09	5.18×10 ⁻¹⁵	95.56	4.69×10 ⁻¹⁵	99.54	1.58×10 ⁻¹⁵	94.68	2.32×10 ⁻¹⁷	98.32	2.97×10 ⁻¹⁸	99.46	1.70×10 ⁻¹⁷	94.61	3.21×10 ⁻¹⁸	96.64	1.58×10 ⁻¹⁷	99.44	21.2 1.0
1416-01J	1.28	2.15×10 ⁻¹⁵	97.77	1.98×10 ⁻¹⁵	99.67	6.18×10 ⁻¹⁶	96.73	8.89×10 ⁻¹⁸	98.99	1.25×10 ⁻¹⁸	99.60	6.66×10 ⁻¹⁸	96.66	9.71×10 ⁻¹⁹	98.34	6.72×10 ⁻¹⁸	99.58	22.5 2.2
1416-01K	1.49	8.45×10 ⁻¹⁶	98.63	1.76×10 ⁻¹⁵	99.79	3.59×10 ⁻¹⁶	97.91	5.53×10 ⁻¹⁸	99.40	1.12×10 ⁻¹⁸	99.71	3.86×10 ⁻¹⁸	97.85	5.43×10 ⁻¹⁹	99.29	5.97×10 ⁻¹⁸	99.69	15.2 3.3
1416-01L	3.18	1.33×10 ⁻¹⁵	100.00	4.09×10 ⁻¹⁵	100.00	6.51×10 ⁻¹⁶	100.00	1.00×10 ⁻¹⁷	100.00	2.59×10 ⁻¹⁸	100.00	7.01×10 ⁻¹⁸	100.00	4.05×10 ⁻¹⁹	100.00	1.38×10 ⁻¹⁷	100.00	13.3 1.9
Tabor99-15/03																		
1416-03A	0.20	2.84×10 ⁻¹⁵	5.23	5.44×10 ⁻¹³	23.78	3.63×10 ⁻¹⁶	2.69	3.55×10 ⁻¹⁶	21.93	3.45×10 ⁻¹⁶	23.83	3.45×10 ⁻¹⁸	2.74	6.30×10 ⁻¹⁸	3.99	1.85×10 ⁻¹⁵	23.92	109.25 112.3
1416-03B	0.25	1.28×10 ⁻¹⁴	28.88	1.27×10 ⁻¹²	79.39	7.33×10 ⁻¹⁶	8.13	8.26×10 ⁻¹⁶	72.92	8.08×10 ⁻¹⁶	79.56	8.08×10 ⁻¹⁸	8.26	9.88×10 ⁻¹⁸	10.25	4.30×10 ⁻¹⁵	79.36	103.0 138.6
1416-03C	0.30	1.38×10 ⁻¹⁵	31.42	2.29×10 ⁻¹³	89.41	7.34×10 ⁻¹⁶	13.57	2.48×10 ⁻¹⁶	82.06	1.45×10 ⁻¹⁶	89.60	1.45×10 ⁻¹⁷	13.79	8.78×10 ⁻¹⁷	65.84	7.78×10 ⁻¹⁶	89.39	10.57 24.52
1416-03D	0.40	4.78×10 ⁻¹⁵	40.22	1.03×10 ⁻¹³	93.95	1.36×10 ⁻¹⁵	23.71	9.21×10 ⁻¹⁷	87.13	6.59×10 ⁻¹⁷	94.15	1.59×10 ⁻¹⁷	24.11	1.02×10 ⁻¹⁷	72.32	3.52×10 ⁻¹⁶	93.91	20.05 5.40
1416-03E	0.50	7.41×10 ⁻¹⁵	53.85	4.87×10 ⁻¹⁴	96.08	2.31×10 ⁻¹⁵	40.89	5.80×10 ⁻¹⁷	90.72	3.09×10 ⁻¹⁷	96.29	2.09×10 ⁻¹⁸	41.57	6.18×10 ⁻¹⁸	76.24	1.66×10 ⁻¹⁶	96.05	18.34 1.96
1416-03F	0.59	7.21×10 ⁻¹⁵	67.12	4.29×10 ⁻¹⁴	97.95	2.67×10 ⁻¹⁵	60.69	5.77×10 ⁻¹⁷	94.28	2.72×10 ⁻¹⁷	98.16	2.72×10 ⁻¹⁸	61.70	3.25×10 ⁻¹⁸	78.30	1.45×10 ⁻¹⁶	97.92	18.50 1.41
1416-03G	0.69	8.16×10 ⁻¹⁵	82.13	2.62×10 ⁻¹⁴	99.10	2.41×10 ⁻¹⁵	78.60	4.74×10 ⁻¹⁷	97.21	1.66×10 ⁻¹⁷	99.31	1.66×10 ⁻¹⁷	79.92	1.40×10 ⁻¹⁷	87.20	8.91×10 ⁻¹⁷	99.07	19.36 1.28
1416-03H	0.84	6.18×10 ⁻¹⁵	93.49	1.31×10 ⁻¹⁴	99.67	1.75×10 ⁻¹⁵	91.56	2.87×10 ⁻¹⁷	98.98	8.33×10 ⁻¹⁸	99.89	8.33×10 ⁻¹⁸	93.10	1.20×10 ⁻¹⁷	94.82	4.44×10 ⁻¹⁷	99.64	20.26 1.10
1416-03I	0.99	2.24×10 ⁻¹⁵	97.63	5.03×10 ⁻¹⁵	99.89	8.07×10 ⁻¹⁶	97.55	1.22×10 ⁻¹⁷	99.73	3.19×10 ⁻¹⁸	100.11	3.19×10 ⁻¹⁸	99.18	5.81×10 ⁻¹⁸	98.51	1.70×10 ⁻¹⁷	99.86	15.97 1.89
1416-03J	2.98	1.32×10 ⁻¹⁵	100.00	2.40×10 ⁻¹⁵	100.00	3.80×10 ⁻¹⁶	100.00	5.40×10 ⁻¹⁸	100.00	1.52×10 ⁻¹⁸	100.00	2.35×10 ⁻¹⁸	100.00	8.43×10 ⁻¹⁸	100.00	20.03	4.50	

a) $J = 0.003193 \pm 0.0000018$; b) cum. %, cumulative percentage.